

Join us.

ScandiDos invites you to a reception to kick-off the AAPM Spring Clinical Meeting while learning more about the **Delta⁴ Discover** and our approval for use with Varian accelerators.

Friday, April 6th, 2018

6:30-8:30pm

JW Marriott Las Vegas Resort & Spa

Cocktails & Appetizers

Presentations by Industry Experts

Bill Salter Ph.D. DABR FAAPM

Director - Radiation Oncology Professor and Chief - Div. of Medical Physics,
Dept. of Radiation Oncology
Huntsman Cancer Institute, University of Utah School of Medicine

Matthew Schmidt

Instructor, Clinical Applications Varian Medical Systems

Görgen Nilsson

CEO/Founder ScandiDos AB

REGISTER

Delta⁴
by ScandiDos

Estimation and validation of patient-specific high-resolution lung elasticity derived from 4DCT

Katelyn Hasse,^{a)} Dylan O'Connell, Yugang Min, John Neylon, Daniel A. Low, and Anand Santhanam

Department of Radiation Oncology, University of California, Los Angeles, CA, USA

(Received 17 August 2017; revised 16 November 2017; accepted for publication 16 November 2017; published 17 December 2017)

Purpose: Lung diseases are commonly associated with changes in lung tissue's biomechanical properties. Functional imaging techniques, such as elastography, have shown great promise in measuring tissue's biomechanical properties, which could expand the utility and effectiveness of radiotherapy treatment planning. We present a novel methodology for characterizing a key biomechanical property, parenchymal elasticity, derived solely from 4DCT datasets.

Methods: Specifically, end-inhalation and end-exhalation breathing phases of the 4DCT datasets were deformably registered and the resulting displacement maps were considered to be ground-truth. A mid-exhalation image was also prepared for verification purposes. A GPU-based biomechanical model was then generated from the patient end-exhalation dataset and used as a forward model to iteratively solve for the elasticity distribution. Displacements at the surface of the lungs were applied as boundary constraints for the model-guided tissue elastography, while the inner voxels were allowed to deform according to the linear elastic forces within the biomechanical model. A convergence criteria of 10% maximum deformation was employed for the iterative process.

Results: The lung tissue elasticity estimation was documented for a set of 15 4DCT patient datasets. Maximum lung deformations were observed to be between 6 and 31 mm. Our results showed that, on average, $89.91 \pm 4.85\%$ convergence was observed. A validation study consisting of mid-exhalation breathing phases illustrated an accuracy of $87.13 \pm 10.62\%$. Structural similarity, normalized cross-correlation, and mutual information were used to quantify the degree of similarity between the following image pairs: (a) the model-generated end-exhalation and ground-truth end-exhalation, and (b) model-generated mid-exhalation images and ground-truth mid-exhalation.

Conclusions: Overall, the results suggest that the lung elasticity can be measured with approximately 90% convergence using routinely acquired clinical 4DCT scans, indicating the potential for a lung elastography implementation within the radiotherapy clinical workflow. The regional lung elasticity found here can lead to improved tissue sparing radiotherapy treatment plans, and more precise monitoring of treatment response. © 2017 American Association of Physicists in Medicine [<https://doi.org/10.1002/mp.12697>]

Key words: 4DCT, biomechanical modeling, lung elastography, lung radiotherapy

1. INTRODUCTION

Lung cancer is the leading cause of cancer-related death worldwide.¹ Lung cancer is usually treated with radiotherapy, but radiotherapy treatment planning is especially difficult for lung cancer because of inherent anatomical and physiological complexity. Many lung diseases, including lung cancer, are associated with changes in lung tissue biomechanical properties.² For instance, pulmonary emphysema and fibrosis are known to be associated with changes in the parenchymal stiffness. Using excised tissue studies, it has been shown that localized changes in the biomechanical properties of lung parenchyma preceded the initiation and progression of certain lung diseases.^{2,3} However, the ability to quantify and localize pulmonary disease onset and progression at a regional level using *in vivo* studies is currently limited. Gold-standard spirometry-based estimates are the current state of the art approach used for overall chronic disease characterization⁴

but do not explicitly characterize regional lung biomechanical information.⁵ While computed tomography (CT), specifically 4DCT, is commonly used for lung radiotherapy imaging and treatment planning purposes, it does not present a quantitative characterization of the lung biomechanical properties.⁶

A critical lung biomechanical property related to parenchymal tissue stiffness is the elastic modulus. Elastography is a noninvasive imaging technique for quantifying the elasticity distribution of the tissue.⁷ Currently, elastography techniques exist across several modalities including MR, ultrasound, and manual palpation.^{8–10} The complexity of the lung anatomy, particularly the air in the lungs, renders current elastography techniques difficult to implement.^{11–14} Additionally, none of the aforementioned imaging techniques are readily available within the radiotherapy workflow.¹⁵

To further the uses of elastography within the radiotherapy context, this paper investigates the application of elastography using 4DCT scans of the human lung. We hypothesize

that such an approach will enable lung tissue elastic properties to be estimated using conventional radiotherapy imaging modalities. A critical step in furthering the uses elastography within the radiotherapy context is the need to quantitatively validate the lung elasticity measurements. Once validated, these properties can be used for advancing lung cancer treatment planning and delivery, and monitoring treatment response.

Our lung elastography process focused on identifying an effective Young's modulus (E) for each voxel of lung tissue on a 4DCT scan. The approach was based on modeling the lung tissue behavior during breathing. Using a well-established, linear elastic constitutive model, we mathematically formulated the lung tissue elasticity estimation as an inverse problem that was solved with an iterative optimization of the elasticity distribution.^{16,17}

The ground-truth tissue behavior was characterized from the 4DCT datasets. 4D displacement vector fields (DVF) obtained from deformable image registration were employed as a boundary constraint to guide the elastography process.¹⁸ A key component of this paper is the quantitative validation of the estimated lung elastography distributions. As 4DCT scans have data for every phase of the breathing cycle, validation is performed by analyzing mid-exhalation.

The rest of the paper is organized as follows: Section 2 introduces the methods employed for the elastography and the validation processes. Section 3 presents the qualitative results of the deformable image registration, elastography, and validation process, while Section 4 presents a numerical analysis of the results. Section 5 presents a discussion of the results and highlights the areas for continued research, and Section 6 concludes the paper.

2. METHODS

Our elastography process focused on the effective Young's modulus (E) estimation for each voxel of lung tissue using 4DCT lung data. Figure 1 shows a flowchart summarizing the elasticity estimation. First, the end-inhalation and the end-exhalation breathing phases from the 4DCT lung images were registered using an optical flow deformable image registration (DIR) algorithm. The lung DVF was obtained for every voxel of the end-exhalation breathing phase. The biomechanical model was then assembled using the end-exhalation lung geometry along with a random elasticity

distribution as the initial elasticity value. Using the ground-truth lung DVF, the elasticity distribution was optimized. Spatial elasticity and displacement error distributions were obtained and validated (Section 3).

In this section, we first briefly present the DIR technique used to obtain the ground-truth DVF. Next, we present the constitutive model used for representing tissue biomechanics in order to solve the inverse elasticity problem. We then present the optimization process used in the iterative elasticity estimation. This is followed by a discussion of the convergence criteria used for the optimization process. We then describe the image similarity metrics used in our study to characterize the quantitative accuracy of the estimated elasticity combined with the constitutive model. We conclude the section with a discussion of the validation study.

2.A. Deformable image registration

The model-guided elasticity approach presented in this paper relies on displacement values extracted from DIR of 4DCT datasets. The lung is a challenging organ to register and requires DIR due to the large deformation caused by respiration. A patient cohort of 15 4DCT datasets that were acquired using 5DCT protocol (IRB# 11-000620-CR-00004) was employed for the elasticity estimation.^{19–21} The patient cohort consisted of lung cancer patients undergoing SBRT at UCLA. The average age of the patients was 66, six of the patients were male, and nine were female. The 4DCT scans were acquired on Siemens Definition Flash, Siemens Biograph 64, and Siemens Definition AS 64 scanners with 1 mm slice thickness.

The left and right lungs were segmented using an intensity-based thresholding approach.²² Segmented end-inhalation (85th percentile breathing amplitude) were deformably registered to the spatial domain of the end-exhalation (15th percentile breathing amplitude) breathing phases using a well-validated in-house multilevel optical flow DIR algorithm.¹⁸ This registration algorithm has been well-validated for both the lung and head and neck anatomies^{23,24}; therefore, we trust the resulting DVF to be an effective representation of the ground-truth lung motion. The registered DVF for each voxel will be taken to be the effective ground-truth displacement, henceforth denoted as simply ground-truth, for the elasticity estimation process.

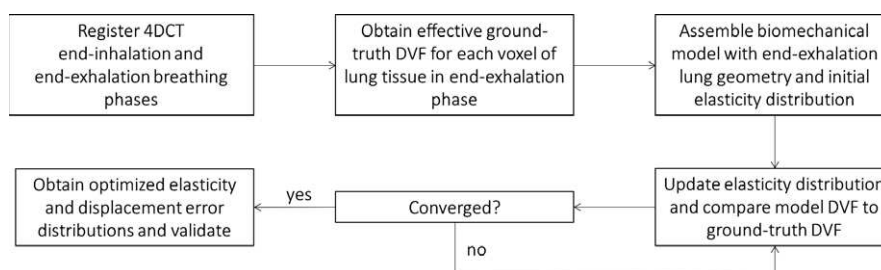


FIG. 1. Flowchart showing 4DCT elasticity estimation process.

2.B. Constitutive model

The model presented in this section is focused on computing the lung tissue deformation for a given lung boundary displacement arising from the ground-truth DVF, as previously demonstrated.²⁵ The model has been previously described in Ref. [26,27] and specifically applied to the lungs.^{28,29} This approach is appropriate for our current study as its applicability has been systematically investigated.²⁹ For clarity purposes, a brief description of the constitutive equations for the forward model²⁷ is presented here.

2.B.1. Model geometry

The biomechanical lung model was assembled from the 4DCT end-exhalation images. The model geometry was represented by finite element nodes corresponding to the center of each voxel in the end-exhalation image. Lung tissue, an elastic material, was viewed as a series of these finite mass elements coupled with linear elastic connections to adjacent mass elements in deformation space. This was to ensure a physically realistic deformation. Rest length and orientation of each connection were then documented and assigned an initial effective Young's modulus and a Poisson's ratio of 0.43.^{30–32}

2.B.2. Model physics

In our approach, linear elastic constitutive laws were implemented because linear elastic representations have been found to be effective in describing normal lung tissue deformations typically observed in 4DCT-based lung motion.³³ Additionally, a study investigating lung tumor motion during external beam radiotherapy found that a hyperelastic constitutive law performed very similarly to linear elastic constitutive law at deformation magnitudes found within the lungs during normal breathing.³²

The model is actuated due to changes in boundary constraints, which subsequently calculates corrective forces on each mass element for given boundary constraints. In our approach, we compute the boundary constraints from the lung boundary DVF. The corresponding corrective forces on each mass element were calculated by summing elastic, shear, and dashpot damping forces for each connected element. The elastic force ($\vec{f}_{E,ab}$) acting between two mass elements a and b is described by:

$$\vec{f}_{E,ab} = \sum_b \left(E_{ab} * \frac{\Delta L_{ab}}{L_{ab}} \right), \quad (1)$$

where E_{ab} is the effective Young's modulus acting between the two elements a and b , and L_{ab} is the rest length distance, and ΔL_{ab} is the change in length between the two elements. As lung tissue is modeled as a linearly elastic material, (1) is derived from the inverse relationship between Young's modulus and displacement; for a constant force, if elastic modulus increases then displacement must decrease and vice versa.¹⁷

The shear spring force ($\vec{f}_{S,ab}$) on element a due to element b is described by

$$\vec{f}_{S,ab} = \sum_b \left(S_{ab} * \frac{L_{ab} - \Delta L_{ab}}{L_{ab}} \right), \quad (2)$$

where S_{ab} is the shear moduli between element a and b , set to 4 kPa for each voxel in our estimations, an approximation based on the relationship between shear modulus, Young's modulus, and Poisson's ratio and similar to values seen in Ref. [34,35]. The dashpot damping force is calculated from the relative velocities \vec{v} of elements a and b , and a local damping factor μ_{ab} .

$$\vec{f}_{v,ab} = \sum_b (\mu_{ab} * (\vec{v}_b - \vec{v}_a)). \quad (3)$$

The new positions and velocities of each mass element (\vec{x}_a^{n+1} , \vec{v}_a^{n+1}) were then updated from the previous values (\vec{x}_a^n , \vec{v}_a^n) using Implicit Euler integration and the total internal corrective force \vec{f}_a .

$$\vec{v}_a^{n+1} = \vec{v}_a^n + \left(\frac{\vec{f}_a}{m_a} + \vec{g} \right) \delta, \quad (4)$$

$$\vec{x}_a^{n+1} = \vec{x}_a^n + \vec{v}_a^{n+1} \delta. \quad (5)$$

In (4) and (5), δ is the time step between iteration, m_a is the mass of each mass element a , and \vec{g} is the acceleration due to gravity. The distance between the new and previous positions of each mass element was taken to be the displacement for that mass element, henceforth denoted as d_a .

2.C. Inverse elasticity formulation

For clarity, the simplifying notation that will be used in this paper is listed in Table I.

The inverse elasticity problem was formulated as a parameter-optimization problem with an objective to determine the elasticity parameter that would minimize the difference between the ground-truth DVFs ($DVF_{DIR,A}$) and those computed by the constitutive model. Solving this inverse elasticity problem was carried out in two steps: (a) estimating the DVF for every voxel of tissue for a given elasticity distribution and changes in boundary constraints, and (b) optimizing the elasticity distribution to best reproduce the $DVF_{DIR,A}$.

TABLE I. Notation and description for resultant terms utilized in the manuscript.

Notation	Description
$DVF_{DIR,A}$	Ground-truth end-exhalation to end-inhalation DIR DVFs
$DVF_{DIR,B}$	Ground-truth end-exhalation to mid-exhalation DIR DVFs
$DVF_{Model,A}$	Model-generated end-exhalation to end-inhalation DVFs
$DVF_{Model,B}$	Model-generated end-exhalation to mid-exhalation DVFs
E_A	Effective elasticity distribution obtained from minimizing error between $DVF_{DIR,A}$ and $DVF_{Model,A}$.

In the first step, we applied the lung boundary conditions, and the interior mass elements were allowed to deform according to the elastic constitutive forces within the model, described in Section B above. For the second step, the iterative scheme for estimating the elastic distribution is based on the inverse relationship between Young’s modulus and displacement. Given an initial Young’s modulus distribution, the constitutive model computed mass element displacements.³⁶ These displacements were then compared with $DVF_{DIR,A}$, and the effective Young’s modulus was iteratively updated until the difference between the above two displacement maps was minimal. New displacements values were generated for each iteration by updating the effective Young’s modulus distribution as described below.

Initial (E_a), minimum ($E_{min,a}$), and maximum ($E_{max,a}$) Young’s modulus values were initialized for each voxel a in the biomechanical model. For lung elastography purposes, the Young’s modulus range was set to be from 1 to 20 kPa, an extended approximation of values from the literature.³⁷ The displacement differential was calculated according to the following relationship:

$$\Delta d_a = \|d_{0,a} - d_a\|, \tag{6}$$

where $d_{0,a}$ and d_a refer to the ground-truth and model-generated displacements of voxel a , respectively. The displacement differential was then used to binaurally update the $E_{min,a}$ and $E_{max,a}$:

$$\text{if } \Delta d_a < 0 : \begin{cases} E_{min,a} = E_a \\ E_{max,a} = E_{max,a} \end{cases}, \tag{7}$$

$$\text{if } \Delta d_a > 0 : \begin{cases} E_{min,a} = E_{min,a} \\ E_{max,a} = E_a \end{cases}. \tag{8}$$

A new E'_a , which became the initial value for the next iteration, was then generated at each iteration according to the modified Gauss–Newton optimization scheme³⁸ with a step size

$$\Delta E_a = (E_{max,a} - E_{min,a}), \tag{9}$$

$$E'_a = E_a + \Delta E_a. \tag{10}$$

After the elasticity was updated, the biomechanical model was then reset to the initial undeformed rest position, and the boundary constraints were reapplied. The reconstruction process was repeated until a suitable stopping (convergence) criteria was reached. Upon convergence, the resultant elasticity estimation (E_A) is recorded along with the resultant deformation vector for each voxel ($DVF_{Model,A}$).

2.D. Convergence metrics

The convergence metrics utilized in this study are a critical component to interpreting the results. At each iteration of the elasticity estimation, the resultant model DVF, $DVF_{Model,A}$, were compared to $DVF_{DIR,A}$. The number of voxels that converged within a certain ϵ value of ground-truth was quantified as follows:

$$c_a = \begin{cases} 1 : & \| |d_a| - |d_{a,0}| \| < \epsilon \\ 0 : & \text{otherwise} \end{cases} \tag{11}$$

$$p_\epsilon = \frac{\sum_1^n c_a}{n}. \tag{12}$$

In (11), (ϵ) represents the L2-norm of the DVF for each voxel a and c_a represents the error for each voxel. The percent accuracy p_ϵ was then tabulated by summing the c_a over all n voxels in lung volume V using (11) and (12). For elastography purposes, the iterative process was stopped when $p_\epsilon \geq 0.95$. The maximum iteration limit was set to be 100.

Factors that impact the convergence criteria are determined by image resolution and range of DVF values. In our case, the image resolution was limited to 1 cubic mm, which led to a $\epsilon_1 = 1$ mm. Image resolution is also impacted by the signal in the underlying tissue. Higher signal-to-noise (SNR) is generally observed in blood vessels due to the high contrast and constant structure during deformation, while parenchymal tissue exhibits lower SNR. For this reason, accuracy will be considered for voxels representing blood vessels and parenchymal tissue separately. The voxels representing the two substructures were segmented using an intensity threshold of -500 HU.³⁹

As lung deformation can vary widely between patients and breathing phases, we also formulated a convergence criteria, where the percent of voxels converged within 10% of the minimum deformation, or $\epsilon_2 = 0.1 * \max_a(|d_a|)$. For each 4DCT dataset, we computed the minimum value among ϵ_1 and ϵ_2 , and employed that for the optimization process. However, once the elasticity estimation converged, the results were evaluated according to both convergence criteria.

2.E. Image similarity metrics for quantitative evaluation

While the convergence criteria provided a quantitative way to assess the elasticity estimation accuracy, an additional metric was necessary to ensure the precision of the estimated elasticity. Specifically, we wanted to ensure that E_A and $DVF_{Model,A}$ could be used to warp the end-exhalation image to closely represent the end-inhalation image. In addition, the usage of image similarity metrics could quantify the accuracy of the ground-truth data. The image similarity metrics will be quantified for both the estimation and validation datasets. The results will be compared for significant difference using the Student’s t -test. For this purpose, three different image similarity metrics were utilized.

2.E.1. Structural similarity index metric

The structural similarity index metric (SSIM) was the first image similarity metric we investigated. SSIM has been previously investigated for the lung, and examines structural changes that more closely correlate with a visual evaluation rather than differences that do not contribute to perceived image quality, which is important for lung.^{40–42}

The SSIM⁴³ is formulated as follows:

$$SSIM(x, y) = \frac{(2\mu_x\mu_y + c_1)(2\sigma_{xy} + c_2)}{(\mu_x^2 + \mu_y^2 + c_1)(\sigma_x^2 + \sigma_y^2 + c_2)} \quad (13)$$

The SSIM can vary between -1 and 1 , where a score of 1 indicates perfect similarity using the equation below. The parameters of (13) include spatial patches extracted from two images x and y , the mean of the voxel intensities in x and y (μ), the variance of the intensities in the x and y (σ), and the covariance (σ_{xy}).

2.E.2. Normalized cross-correlation

Another image similarity metric that was used to assess the results of our study was normalized cross-correlation (NCC). NCC is a simple but effective similarity measure that is invariant to brightness and contrast variations.⁴⁴ NCC has been previously used to compare similarity of medical lung images in⁴⁴ and has the advantage that it is less sensitive to linear changes in amplitude of grayscale values. NCC is often used to overcome intensity changes caused by tissue compression difference between different breathing phases.⁴⁵ Like SSIM, NCC values range from a perfect match of 1 to a completely anticorrelated match of -1 . The equation for calculating the NCC is shown as

$$NCC(x, y) = C_{xy}(\hat{x}, \hat{y}) = \sum_{i,j \in R} \hat{x}(i, j) \hat{y}(i, j), \quad (14)$$

where \hat{x} and \hat{y} are intensity normalized warped end-exhalation and end-inhalation images.

2.E.3. Mutual information

The final image similarity metric that we used was mutual information (MI), which is a symmetric and nonnegative similarity measure of entropy between two images that takes high

values for similar images. Maximization of MI indicates complete correspondence between two images. MI assumes no prior functional relationships between the images, but rather a statistical relationship that can be evaluated by analyzing the images' joint entropy.⁴⁶ Although MI is normally applied to multimodal registration, it is often commonly used for lung alignment.⁴⁷

Assuming two images x and y , the mutual information is computed by comparing the image entropy values (i.e., a measure of how well-structured the common histogram is) allows:

$$MI(x, y) = H(x) + H(y) - H(x, y) \quad (15)$$

where $H(x, y)$ is the joint entropy

$$- \sum_{x,y} p_{xy}(x, y) \log p_{xy}(x, y) \quad (16)$$

and $H(x)$ and $H(y)$ are the individual entropies

$$- \sum_x p_x(x) \log p_x(x). \quad (17)$$

2.F. Validation study

A key part of our focus is to validate the estimated elasticity using clinical datasets. However, patient-specific elasticity distributions have not been previously documented in the literature. For quantitative validation purposes, we employed a mid-exhalation breathing phase from the 4DCT dataset that was not used for the elasticity reconstruction. An illustration of the lung deformation differences seen between the estimation dataset and the validation dataset is shown in Fig. 2 below. The end-exhalation segmented CT is shown in (a). Figure 2(b) shows the magnitude of displacement between the end-exhalation and end-inhalation breathing phases used in the elasticity estimation, while Fig. 2(c) shows the magnitude of displacement between the end-exhalation and mid-exhalation breathing phases used in the validation study.

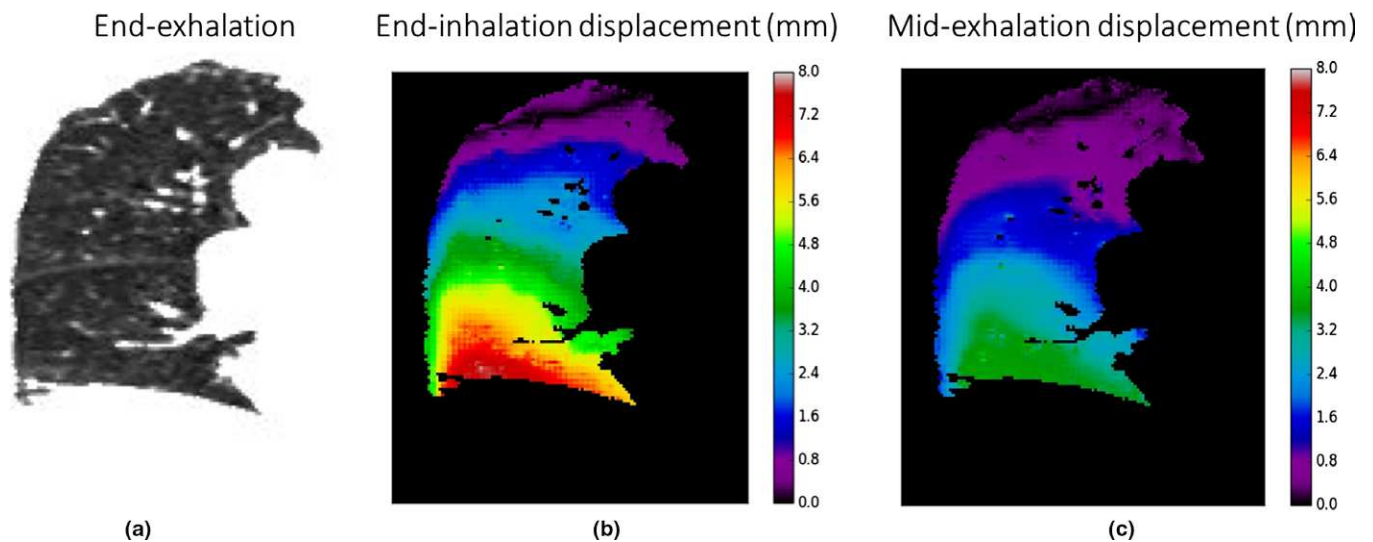


FIG. 2. Comparison of the breathing phases utilized for elasticity estimation. Source end-exhalation image is shown in (a). The displacement between end-exhalation and end-inhalation is shown in (b), and the displacement between end-exhalation and mid-exhalation is shown in (c) with the same colorbar. [Color figure can be viewed at wileyonlinelibrary.com]

The accuracy of the elasticity distribution E_A derived from end-inhalation breathing data was quantified by its ability to also represent the mid-exhalation breathing data. Specifically, the mid-exhalation breathing image dataset was first registered to the end-exhalation breathing phase using the optical flow DIR algorithm. These DVFs were then recorded as $DVF_{DIR,B}$. The elasticity information (E_A) estimated using $DVF_{DIR,A}$ was applied to the biomechanical lung model according to the boundary conditions described in Section 2.A.2 with lung surface displacement now prescribed by $DVF_{DIR,B}$, which generated $DVF_{Model,B}$. The $DVF_{Model,B}$ were then compared to the $DVF_{DIR,B}$, and the accuracy was reported according to the convergence criteria (Section 2.D). As an alternative means of quantifying and describing the validation results, image similarity measures (Section 2.E) were employed to compare end-exhalation images warped with both $DVF_{DIR,B}$ and $DVF_{Model,B}$ to the validation mid-exhalation images. Our hypothesis is that the image similarity measures for the $DVF_{DIR,B}$ and $DVF_{Model,B}$ will be similar to those of $DVF_{DIR,A}$ and $DVF_{Model,A}$.

2.G. Implementation details

The computational complexity of iteratively updating high-resolution finite element model²⁷ until convergence was countered using a GPU cluster that consisted of 32 NVIDIA TitanX GPUs interconnected by an Infiniband backbone. The GPU cluster allowed the elasticity estimation for each patient lung dataset to converge in around 2 h of computation time. The numpy and scikit packages of Python 2.7 were used numerical analysis in this manuscript.⁴⁸

3. QUALITATIVE RESULTS

In this section, we first present the qualitative DIR results, followed by the elasticity estimation results for all the 15 datasets. Finally, we present the qualitative results of the validation process.

3.A. Deformable image registration

The accuracy of the DIR results is critical in order to ensure the DIR's validity as ground-truth data for the elastography procedure. Figure 3 illustrates an example of the deformable image registration results for a 2D-slice of the left (a & b) and right (c & d) lung. Figures 3(a) & 3(c) show an overlay of the end-exhalation image in green and end-inhalation image in red. The misalignments between slices are depicted in red (features that are only seen in end-inhalation image) and green (features that are only seen in the end-exhalation image). Significant motion can be observed between the two images in each case. Figures 3(b) and 3(d) show an overlay of the end-exhalation image warped using $DVF_{DIR,A}$, and the end-inhalation, illustrating the high accuracy at which our in-house optical flow DIR algorithm can calculate DVFs. The maximum $DVF_{DIR,A}$ was observed to be between 6 and 31 mm, while the maximum $DVF_{DIR,B}$ was observed to be between 2 and 10 mm.

3.B. Elasticity estimation results and accuracy

Over all 15 patient lung datasets, $89.91 \pm 4.85\%$ of voxels converged within ϵ_2 . To illustrate elasticity results and correlate these results to displacement accuracy, Figure 4 show the displacement accuracy corresponding with a resultant elasticity map for a 2D-slice of a left patient lung.

Figure 4(a) shows the ground-truth displacement in mm ($DVF_{DIR,A}$), while Fig. 4(b) shows the model displacement also in mm ($DVF_{Model,A}$). Figure 4(c) shows the displacement error between 4(a) and 4(b), with error greater than 1 mm (ϵ_1) highlighted in purple and error greater than 1.2 mm (ϵ_2) highlighted in blue. Finally, Fig. 4(d) shows the optimized elasticity map, E_A , in kPa. It can be seen that the $DVF_{DIR,A}$ and $DVF_{Model,A}$ are very similar, with low error illustrated in Fig. 4(c). The minimal displacement error supports the validity of the elasticity estimated for this case. Regions of low motion correspond to regions of lower elasticity; this is due to our underlying assumption guiding the elasticity update

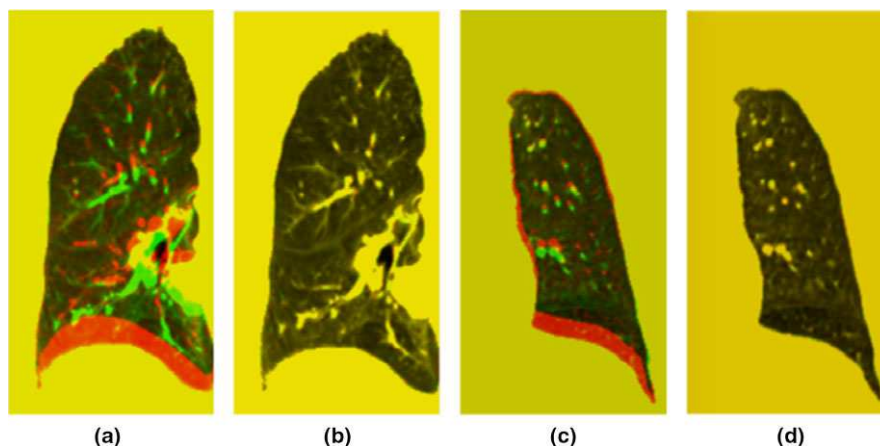


FIG. 3. Deformable image registration results for sample left (a and b) and right (c and d) 2D lung slice. (a and c) illustrate an overlay of end-exhalation and end-inhalation (b and d) overlay of warped end-exhalation and end-inhalation. [Color figure can be viewed at wileyonlinelibrary.com]

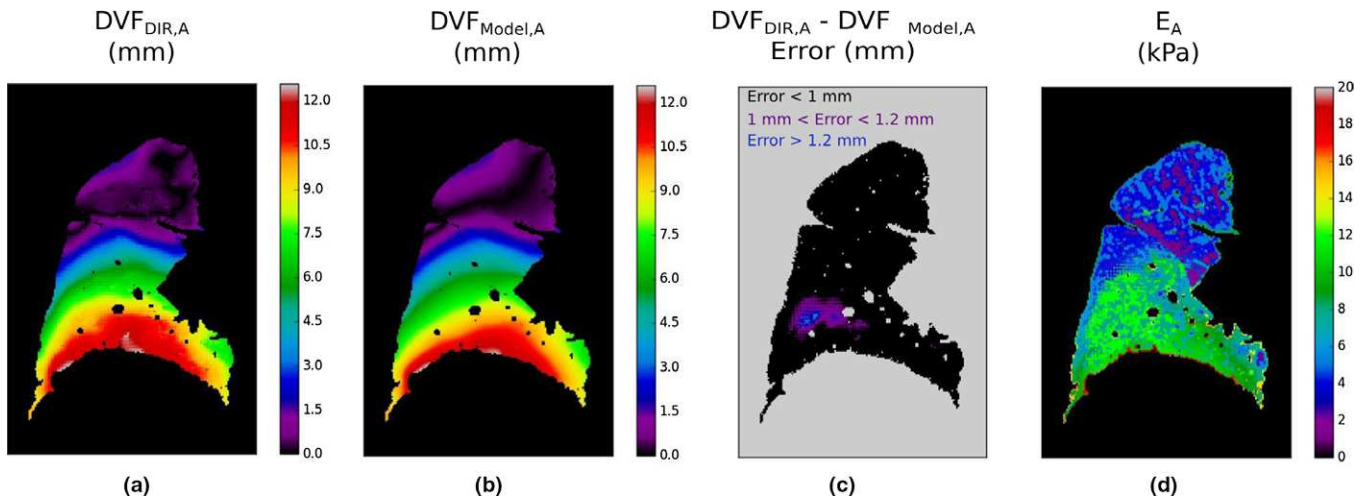


FIG. 4. 2D-slice illustrating (a) ground-truth displacement $DVF_{DIR,A}$, (b) model displacement $DVF_{Model,A}$, (c) displacement error between (a) and (b) with error greater than ϵ_1 and ϵ_2 highlighted respectively and (d) resultant elasticity distribution. [Color figure can be viewed at wileyonlinelibrary.com]

process. Though the displacement distributions are relatively smooth, the resultant elasticity distribution varies from voxel to voxel. As no ground-truth elasticity distributions are available for absolute elasticity accuracy calculations, validation was performed using mid-exhalation breathing phase 4DCT data. The results of the validation process will be qualitatively evaluated in the following section.

3.C. Validation

On average, the validation datasets converged with $87.13 \pm 10.62\%$ of voxels within ϵ_1 . To illustrate the validation process and results, we present Fig. 5. Figure 5(a) shows the $DVF_{DIR,A}$ for a 2D slice of the right lung in mm. Figure 5(b) shows the E_A estimated from the $DVF_{DIR,A}$ in 5(a) for the corresponding slice. The validation displacement for a 2D slice of the right lung ($DVF_{DIR,B}$) is shown in mm in Fig. 5(c). Figure 5(d) shows the resultant model displacement in mm after the lung biomechanical model is deformed with the E_A seen in Fig. 5(b) ($DVF_{Model,B}$). Figure 5(e)

illustrates the displacement error between 5(c) and 5(d), with error greater than 0.4 mm, ϵ_2 , highlighted in blue. While a cluster in the center of the slice shown in 5(c) had error higher than ϵ_2 , a majority of the voxels converged with a high accuracy, illustrating the estimated elasticity’s validity in representing the $DVF_{DIR,B}$. The decrease in ϵ_2 due to the decrease in maximum lung displacement can also explain the higher error seen in Fig. 5(c). The results will be analyzed further in the following section.

4. QUANTITATIVE EVALUATION

In this section, we first present the image similarity measures for the DIR, followed by a numerical analysis of the elasticity estimation and validation results.

4.A. DIR

The quantitative image similarity of the DIR was documented for two image pairs: (a) the $DVF_{DIR,A}$ -warped end-

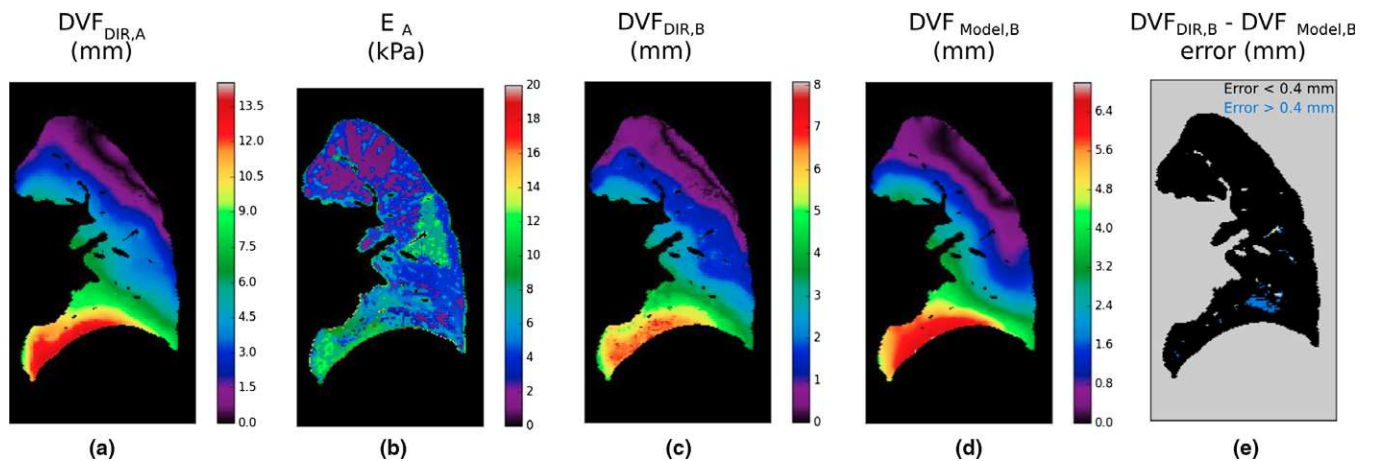


FIG. 5. 2D-slice illustrating (a) end-inhalation ground-truth displacement $DVF_{DIR,A}$ in mm, (b) estimated elasticity in kPa, (c) mid-exhalation ground-truth $DVF_{DIR,B}$ in mm, (d) mid-exhalation model $DVF_{Model,B}$ in mm, and (e) error between (a) and (b) with error greater than 0.4 mm highlighted. [Color figure can be viewed at wileyonlinelibrary.com]

exhalation and end-inhalation images, and b) $DVF_{DIR,B}$ -warped end-exhalation and mid-inhalation images. Table II summarizes the results for both (a) and (b), respectively.

On average for (a), image pairs had an SSIM of 0.88, NCC of 0.99, and an MI of 1.94, indicating a high similarity. This illustrates the high accuracy of the $DVF_{DIR,A}$ that were used as ground-truth throughout the elastography process. For the validation DIR (b), image pairs had an average SSIM of 0.89, NCC of 0.99, and MI of 1.81. These numbers are not significantly different ($P > 0.05$) from the SSIM, NCC, and MI values of (a), confirming our hypothesis and illustrating the accuracy of the $DVF_{DIR,B}$ used to validate the elastography process.

4.B. Elasticity estimation results and accuracy

The quantitative results of our elasticity estimation for the 15 patient lung datasets are now presented. Table III indicates the average elasticity, displacement, displacement error, and e_2 accuracy for each patient lung dataset. Overall, $89.91 \pm 4.85\%$ of voxels converged within the prescribed e_2 . All patient datasets converged with greater than 80% of voxels within e_1 or e_2 . The average elasticity ranged from 4.91 to 7.66 kPa. Variations in the lung physiological factors, such as range of motion and total lung volume, did not affect the accuracy, indicating the applicability of the elastography process to a wide range of patients.

As mentioned in Section 2.D, two convergence criteria were investigated to better quantify the accuracy of the model-generated elasticity. Table IV denotes the e_1 and e_2 convergence percentages broken down by underlying tissue types for the 15 4DCT patient datasets. Maximum

TABLE II. Image similarity metrics SSIM, NCC, and MI for patient end-inhalation to end-exhalation registration as well as validation end-inhalation to mid-exhalation registration.

ID	$DVF_{DIR,A}$ -warped end-exhalation and end-inhalation			$DVF_{DIR,B}$ -warped end-exhalation and mid-inhalation		
	SSIM	NCC	MI	SSIM	NCC	MI
1	0.90	0.99	1.92	0.91	0.98	2.01
2	0.88	0.98	2.01	0.88	0.98	2.00
3	0.88	0.99	2.01	0.89	0.99	1.95
4	0.86	0.99	2.01	0.88	0.99	2.14
5	0.83	0.98	2.14	0.86	0.96	1.81
6	0.86	0.99	2.04	0.88	0.99	1.76
7	0.87	0.98	1.91	0.88	0.98	1.64
8	0.87	0.99	1.86	0.89	0.99	1.63
9	0.91	0.99	1.73	0.93	0.99	1.69
10	0.87	0.99	2.07	0.87	0.99	1.97
11	0.88	0.99	1.85	0.89	0.99	1.72
12	0.90	0.99	1.61	0.92	0.99	1.49
13	0.88	0.99	2.03	0.89	0.99	1.79
14	0.88	0.99	1.96	0.90	0.99	1.70
15	0.87	0.99	1.87	0.88	0.99	1.66
Av	0.87	0.99	1.94	0.89	0.99	1.80

TABLE III. Average elasticity, displacement, error, and overall accuracy for each patient investigated in this study.

ID	Average elasticity (kPa)	Average displacement (mm)	Average error (mm)	Average ϵ_2 accuracy (%)
1	7.66	5.22	0.74	89.43
2	5.87	1.62	0.23	97.75
3	6.23	2.14	0.40	90.64
4	4.91	2.39	0.38	94.37
5	7.07	6.41	0.91	92.63
6	6.37	4.14	0.68	84.38
7	6.72	4.30	0.72	85.01
8	6.79	4.76	0.75	89.39
9	6.45	4.12	0.83	83.68
10	5.17	4.84	0.62	90.78
11	5.37	3.09	0.78	80.95
12	6.14	4.96	0.63	94.26
13	7.25	3.93	0.61	92.53
14	6.20	5.01	0.81	87.29
15	5.46	3.11	0.44	95.55
Avg	6.24	4.00	0.63	89.91

TABLE IV. Voxel convergence and maximum deformation for a sample of patient 4DCT datasets.

ID	Blood Vessels			Parenchyma	
	Max $DVF_{Model,A}$ (mm)	ϵ_1 accuracy (%)	ϵ_2 accuracy (%)	ϵ_1 accuracy (%)	ϵ_2 accuracy (%)
1	20.30	80.85	90.32	78.93	89.32
2	6.31	98.03	86.86	97.74	85.51
3	8.58	93.83	92.02	89.26	85.63
4	12.12	94.03	95.83	90.96	94.30
5	26.31	75.73	93.87	71.74	92.47
6	14.85	89.31	93.10	75.17	83.89
7	15.68	85.75	90.55	74.07	84.70
8	19.97	87.12	92.52	79.69	89.18
9	17.32	85.33	90.49	69.24	83.41
10	16.99	90.19	95.24	76.72	90.61
11	18.58	95.16	98.27	89.55	98.12
12	20.32	88.25	95.29	79.38	94.20
13	15.53	82.37	90.90	78.58	92.82
14	21.11	82.68	91.00	73.72	87.08
15	15.59	94.20	97.27	88.14	95.43
Av	16.57	88.19	92.91	80.86	89.77

deformation has also been included in the table to illustrate the difference in deformation between patients. It can be seen that the voxels representing blood vessels had a slightly higher accuracy than the parenchymal voxels, though it was not significant when looking at the accuracy with regard to e_2 . The higher accuracy can be attributed to the higher signal-to-noise ratio in the blood vessels when compared to the parenchymal tissue. This illustrates that though local image

noise contributes toward estimation error as expected, the accuracy of the parenchymal tissue is still within a clinically applicable error range.

The SSIM, NCC, and MI metrics were used to quantify the similarity between the ground-truth end-inhalation and $DVF_{Model,A}$ -deformed end-exhalation images. Table V shows the SSIM, NCC, and MI for these results. On average, the end-inhalation and $DVF_{Model,A}$ -deformed end-exhalation images had an SSIM of 0.89, NCC of 0.97, and an MI of 1.83, indicating high similarity regardless of structural or intensity changes between end-exhalation and end-inhalation images. These numbers were not significantly different from the DIR results shown in Table II, indicating that the accuracy of the elasticity estimation correlates to the accuracy of the underlying ground-truth data.

4.C. Validation

The quantitative results of the validation study for the 15 patient lung datasets are now presented. On average, the validation datasets converged with $87.13 \pm 10.62\%$ of voxels within. Table VI denotes the convergence percentages reported according to the two different ϵ values for the validation datasets. The convergence percentages have been separated based on the underlying tissue types. The maximum deformation is also shown.

When compared to Table IV, Table VI shows differences in maximum deformation values. On average, the deformation between end-inhalation and end-exhalation breathing phases was 16.57 mm, while the deformation between end-inhalation and mid-exhalation was 6.51 mm. Because the maximum deformation was significantly lower for the validation datasets, the ϵ_2 accuracy decreased. As seen in Table IV, the blood vessels had higher accuracy than the parenchymal

TABLE V. Image similarity metrics SSIM, NCC, and MI comparing patient ground-truth end-inhalation images to $DVF_{Model,A}$ -deformed end-exhalation images.

ID	SSIM	NCC	MI
1	0.95	0.99	1.85
2	0.91	0.97	1.97
3	0.91	0.98	1.86
4	0.87	0.96	2.12
5	0.92	0.98	1.97
6	0.90	0.98	1.94
7	0.92	0.98	1.88
8	0.92	0.99	1.90
9	0.91	0.98	1.73
10	0.93	0.99	2.12
11	0.90	0.97	1.74
12	0.94	0.99	1.54
13	0.92	0.99	1.93
14	0.92	0.98	1.81
15	0.92	0.98	1.61
Av	0.92	0.98	1.86

TABLE VI. Convergence percentages for validation datasets.

ID	Blood vessels			Parenchyma	
	Max $DVF_{Model,B}$ (mm)	ϵ_1 accuracy (%)	ϵ_2 accuracy (%)	ϵ_1 accuracy (%)	ϵ_2 accuracy (%)
1	4.90	96.17	88.44	92.31	77.01
2	2.24	94.93	84.92	90.87	56.41
3	3.34	93.74	84.38	82.48	58.64
4	4.14	88.13	77.06	78.86	50.81
5	8.85	89.90	87.99	94.77	92.70
6	4.83	96.47	90.49	95.00	75.34
7	9.56	87.88	74.08	72.13	70.10
8	7.08	85.97	83.77	69.06	62.89
9	6.94	83.20	77.40	69.64	58.20
10	8.58	86.31	85.40	55.45	51.88
11	8.50	97.11	97.31	89.63	89.33
12	9.83	85.07	85.42	71.15	71.11
13	5.81	98.39	91.79	96.36	79.63
14	7.26	94.06	89.60	83.67	72.21
15	5.72	96.16	93.04	99.04	97.66
Av	6.51	91.57	86.07	82.70	70.93

tissue. Again, this can be explained by the higher signal-to-noise ratio in the blood vessels as compared to the parenchymal tissue. This indicates that the validation error is still skewed by the underlying image quality, which is consistent with the initial results. However, the significantly smaller magnitudes of $DVF_{DIR,B}$ exerted more influence on the overall accuracy of the elasticity estimation than the SNR.

Finally, image similarity was investigated for the validation results. Table VII shows the SSIM, NCC, and MI results for the validation model. The end-inhalation and $DVF_{Model,B}$ -

TABLE VII. Image similarity metrics SSIM, NCC, and MI comparing validation mid-exhalation images to $DVF_{Model,B}$ -deformed end-exhalation images to $DVF_{Model,A}$ -deformed end-exhalation images2.

ID	SSIM	NCC	MI
1	0.87	0.97	1.90
2	0.72	0.86	1.96
3	0.79	0.91	1.88
4	0.72	0.91	1.86
5	0.92	0.99	1.71
6	0.80	0.98	2.00
7	0.80	0.93	1.73
8	0.79	0.90	1.75
9	0.77	0.95	2.00
10	0.76	0.93	2.16
11	0.88	0.96	1.61
12	0.86	0.98	1.78
13	0.78	0.97	2.05
14	0.83	0.98	1.93
15	0.86	0.98	1.77
Av	0.81	0.95	1.87

deformed mid-exhalation images had an SSIM of 0.80, NCC of 0.95, and an MI of 1.85. These numbers are not significantly different from the image similarity achieved in Table V ($P > 0.05$), validating the accuracy and robustness of the elasticity estimation.

5. DISCUSSION

In this paper, we presented the results of a lung elastography process performed on 15 4DCT patient datasets. A physics-based biomechanical constitutive model was used as a forward model to solve the inverse elasticity problem. Lung DVFs from end-inhalation to end-exhalation breathing phases were obtained from an in-house optical flow DIR algorithm. The lung boundary displacements were then employed as boundary constraints for the forward model, while the inner voxels of the biomechanical model were allowed to deform according to linear elastic material properties.

Using 15 clinical 4DCT datasets, this study indicated that maximum lung deformation ranged from 6 to 31 mm and $89.91 \pm 4.85\%$ of voxels converged within the prescribed metrics. In addition, SSIM, NCC, and MI image similarity metrics showed high similarity between both the end-inhalation and $DVF_{DIR,A}$ -warped end-exhalation registration images, and end-inhalation and $DVF_{Model,A}$ -warped end-exhalation experimental results, with average values of 0.89, 0.98, and 1.90, respectively for the DIR results. Similarly, we observed average values of 0.85, 0.97, and 1.83 for the model-generated results.

The potential of 4DCT-based lung elastography to be used within a clinical radiotherapy workflow required extensive quantitative validation. Mid-exhalation 4DCT datasets were used as validation datasets so that the elasticity results could be validated in a radiotherapy clinically relevant manner. The maximum lung deformation of the validation datasets ranged from 2 to 10 mm, and $87.13 \pm 10.62\%$ of voxels converged within 1 mm of ground-truth deformation. Our results indicated that convergence percentages for each of the subjects during the elastography and validation process were similar, citing the quantitative nature with which the process can be used within the context of clinical radiotherapy. The accuracy was observed to be independent of the subject's lung DVF magnitude, thereby indicating the applicability of such measurements to a wide range of patients and breathing phases. Future work will investigate the acquisition of total lung capacity and functional residual capacity lung scans for validation, as these datasets are independent of 4DCT protocol and could provide the extra benefit of determining degree of hyperinflation and air trapping.

The average elasticity values obtained for the patient cohort ranged from 4.91 to 7.66 kPa. These values are similar to those seen in the literature,³⁷ especially for patients with diseased lungs.⁴⁹ As no ground-truth elasticity distributions are available for accuracy calculations, the accuracy of the elasticity estimation is dependent of the accuracy of the DIR technique and ground-truth DVF values. While we are confident in the capability of our in-house optical flow DIR

algorithm, future work will investigate *in vivo* tissue sample experiments and US/MR elastography techniques for the lung for further verification and validation purposes.

We currently foresee two challenges to the elastography methodology implementation within a radiotherapy setup: image artifacts and computational complexity. Firstly, the lung elastography approach discussed in this paper is sensitive to image artifacts in the 4D image dataset. SNR differences due to the underlying tissue slightly affected the elasticity estimation, though the parenchymal accuracy was still greater than 80%. In this study, a 5D imaging protocol was used to acquire the 4DCT images, which eliminated potential elasticity estimation errors arising from 4D imaging artifacts, irregular breathing, and hyperelastic lung behavior. Though we expect 5DCT methods to become more prevalent, in the future, we will investigate ways to ensure elasticity estimation accuracy for 4DCT datasets that are inherent with image artifacts. We envision machine learning techniques as an approach for predicting initial elastic material properties that will be refined with our biomechanical model.

Secondly, the complexity of the inverse elasticity estimation is a computationally intensive problem. The implementation of the methodology on a GPU cluster allowed for the calculation of patient-specific lung elasticity distributions to be completed in about 2 h. The implementation of these methods and future deep learning methods on a GPU cluster will continue to ensure that the elasticity information will be available within a reasonable radiotherapy timeline.

We foresee a wide range of clinical applications for our elastography method. The novel lung elastography method utilized here is able to directly relate tissue elasticity with the lung tissue deformation derived from clinical radiotherapy datasets. The elasticity information obtained through this methodology can be used to characterize response to radiotherapy and the functionality of the lung tissue on a voxel-by-voxel basis. Functional lung information can lead to patient-specific radiotherapy treatment options. Several authors have reported methods for functional imaging of the lungs for radiation treatment. One example is ventilation imaging, which is generated from the DIR of 4DCT datasets.⁵⁰⁻⁵² Ventilation imaging is based on the Jacobian of DVFs, which describe the lung motion. However, ventilation imaging does not take into account the underlying biomechanical properties of the lung tissue.⁵³ Lung elastography provides critical information about the biomechanical properties of tissue, which have been shown to be related to the underlying lung function and disease. We expect elastography to provide complementary information to current functional imaging techniques. Future work will investigate comparing and integrating elastography and ventilation imaging methods to more fully describe lung function.

Beyond the context of radiotherapy, the elasticity distributions can be used to assess degree of disease in COPD patients, track disease progression, and differentiate between tissue affected by changes in the stiffness, for example, bronchitis and emphysema. Future work will focus on describing and characterizing the lung tissue of patients with different

stages of COPD, obtaining more scan time points, and correlating changes in elasticity over time with radiotherapy and disease progression.

6. CONCLUSION

In this paper, we presented the results of a lung elastography study using 4DCT deformation vectors. Patient-specific ground-truth deformation values between end-inhalation and end-exhalation breathing were obtained for each voxel of lung tissue using optical flow deformable image registration. The methodology employed a constitutive physics-based biomechanical model of the lungs that was iteratively deformed according to patient-specific lung boundary constraints. An inverse analysis consisting of a modified Gauss–Newton-based binary search optimization scheme was utilized to update the spatial elasticity distribution of the lung tissue according to the discrepancy between ground-truth and model deformation. Our analysis showed that an average of $89.91 \pm 4.85\%$ of voxels converged within a prescribed error metric of 10% of maximum deformation. SSIM, NCC, and MI image similarity metrics indicated high similarity between model results and ground-truth deformation. A validation dataset of mid-exhalation breathing phase deformation data converged with $87.13 \pm 10.62\%$ of voxels within 1 mm of ground-truth deformation. These results indicate the quantitative accuracy of the elasticity estimation process. The 4DCT lung elastography methodology investigated here can easily be implemented within a radiotherapy workflow and has potential to improve patient-specific lung cancer radiotherapy treatment options.

ACKNOWLEDGMENTS

This material is based upon work supported by the National Science Foundation Graduate Research Fellowship under Grant No. DGE-1144087 and the UCLA Department of Radiation Oncology.

^{a)}Author to whom correspondence should be addressed. Electronic mail: khasse@mednet.ucla.edu

REFERENCES

1. Society A.C. *Cancer facts and figures*. 2016 [cited 2016].
2. Suki B, Ito S, Stamenovic D, Lutchen KR, Ingenito EP. Biomechanics of the lung parenchyma: critical roles of collagen and mechanical forces. *J Appl Physiol* (1985). 2005;98:1892–1899.
3. Suki B, Bates JH. Extracellular matrix mechanics in lung parenchymal diseases. *Respir Physiol Neurobiol*. 2008;163:33–43.
4. Mikulski MA, Gerke AK, Lourens S, et al. Agreement between fixed-ratio and lower limit of normal spirometry interpretation protocols decreases with age: is there a need for a new GOLD standard? *J Occup Environ Med*. 2013;55:802–808.
5. Brown RH. Registration-based metrics of lung function to describe COPD: the ultimate question of life, the universe, and everything. *Acad Radiol*. 2013;20:525–526.
6. Fredman AJ, Frolik JL, Garra BS. Lung strain profiles using computed tomography elastography. *Conf Proc IEEE Eng Med Biol Soc*. 2004;2:1545–1548.
7. He H, Lu X, Ma H, Zhu J, Huang M. Value of endobronchial ultrasound elastography in the diagnosis of mediastinal and hilar lymph node metastasis in lung cancer. *Zhong Nan Da Xue Xue Bao Yi Xue Ban*. 2016;41:30–36.
8. McGee KP, Hubmayr RD, Levin D, Ehman RL. Feasibility of quantifying the mechanical properties of lung parenchyma in a small-animal model using H-1 magnetic resonance elastography (MRE). *J Magn Reson Imaging*. 2009;29:838–845.
9. Goss BC, McGee KP, Ehman EC, Manduca A, Ehman RL. Magnetic resonance elastography of the lung: technical feasibility. *Magn Reson Med*. 2006;56:1060–1066.
10. Rivaz H, Foroughi P, Fleming I, et al. Tracked regularized ultrasound elastography for targeting breast radiotherapy. *Med Image Comput Comput Assist Interv*. 2009;12:507–515.
11. Sperandio M, Trovato FM, Dimitri L, et al. Lung transthoracic ultrasound elastography imaging and guided biopsies of subpleural cancer: a preliminary report. *Acta Radiol*. 2015;56:798–805.
12. Al-Mayah A, Moseley J, Velec M, Hunter S, Brock K. Deformable image registration of heterogeneous human lung incorporating the bronchial tree. *Med Phys*. 2010;37:4560–4571.
13. Al-Mayah A, Moseley J, Velec M, Brock KK. Sliding characteristic and material compressibility of human lung: parametric study and verification. *Med Phys*. 2009;36:4625–4633.
14. Al-Mayah A, Moseley J, Velec M, Brock K. Toward efficient biomechanical-based deformable image registration of lungs for image-guided radiotherapy. *Phys Med Biol*. 2011;56:4701–4713.
15. O’Shea T, Bamber J, Fontanarosa D, et al. Review of ultrasound image guidance in external beam radiotherapy part II: intra-fraction motion management and novel applications. *Phys Med Biol*. 2016;61:R90–R137.
16. Doyley MM. Model-based elastography: a survey of approaches to the inverse elasticity problem. *Phys Med Biol*. 2012;57:R35–R73.
17. Doyley MM, Meaney PM, Bamber JC. Evaluation of an iterative reconstruction method for quantitative elastography. *Phys Med Biol*. 2000;45:1521–1540.
18. Min YG, Neylon J, Shah A, et al. 4D-CT Lung registration using anatomy-based multi-level multi-resolution optical flow analysis and thin-plate splines. *Int J Comput Assist Radiol Surg*. 2014;9:875–889.
19. Low DA, White BM, Lee PP, et al. A novel CT acquisition and analysis technique for breathing motion modeling. *Phys Med Biol*. 2013;58:L31–L36.
20. Thomas D, Lamb J, White B, et al. A novel fast helical 4D-CT acquisition technique to generate low-noise sorting artifact-free images at user-selected breathing phases. *Int J Radiat Oncol Biol Phys*. 2014;89:191–198.
21. Low DA, Parikh PJ, Lu W, et al. Novel breathing motion model for radiotherapy. *Int J Radiat Oncol Biol Phys*. 2005;63:921–929.
22. Ung YC, Wu K, Hornby J, et al. Defining the appropriate PET intensity threshold and CT threshold for target delineation in early stage non-small cell lung cancer: a radiological and pathological correlation study. *Int J Radiat Oncol Biol Phys*. 2008;72:S113–S113.
23. White BM, Vennarini S, Lin L, et al. Accuracy of routine treatment planning 4-dimensional and deep-inspiration breath-hold computed tomography delineation of the left anterior descending artery in radiation therapy. *Int J Radiat Oncol Biol Phys*. 2015;91:825–831.
24. Dou TH, Min YG, Neylon J, et al. Fast simulated annealing and adaptive Monte Carlo sampling based parameter optimization for dense optical-flow deformable image registration of 4DCT lung anatomy. In *SPIE Medical Imaging 2016: Image-Guided Procedures, Robotic Interventions, and Modeling*; 2016: 9786.
25. Villard PF, Beuve M, Shariat B, Baudet V, JAILLET F. Simulation of lung behaviour with finite elements: influence of bio-mechanical parameters. In: *Third International Conference on Medical Information Visualisation - BioMedical Visualisation (MediVis 2005), Proceedings*; 2005: 9–14.
26. Hasse K, Neylon J, Sheng K, Santhanam AP. Systematic feasibility analysis of a quantitative elasticity estimation for breast anatomy using supine/prone patient postures. *Med Phys*. 2016;43:1299–1311.
27. Neylon J, Qi X, Sheng K, et al. A GPU based high-resolution multilevel biomechanical head and neck model for validating deformable image registration. *Med Phys*. 2015;42:232–243.
28. Santhanam AP, Imielinska C, Davenport P, Kupelian P, Rolland JP. Modeling real-time 3-d lung deformations for medical visualization. *IEEE Trans Inf Technol Biomed*. 2008;12:257–270.

29. Hasse K, Neylon J, Santhanam AP. Feasibility and quantitative analysis of a biomechanical model-guided lung elastography for radiotherapy. *Biomed Phys Eng Express*. 2017;3:025006.
30. Al-Mayah A, Moseley J, Brock KK. Contact surface and material nonlinearity modeling of human lungs. *Phys Med Biol*. 2008;53:305–317.
31. Liu F, Tschumperlin DJ. Micro-mechanical characterization of lung tissue using atomic force microscopy. *J Vis Exp*. 2011;54:2911.
32. Karami E, Gaede S, Lee TY, Samini A. A biomechanical approach for in vivo lung tumor motion prediction during external beam radiation therapy. In: *SPIE Proceedings: Medical Imaging 2015: Image-Guided Procedures, Robotic Interventions, and Modeling*; 2015: 9415.
33. Diciotti S, Nobis A, Ciulli S, et al. Development of digital phantoms based on a finite element model to simulate low-attenuation areas in CT imaging for pulmonary emphysema quantification. *Int J Comput Assist Radiol Surg*. 2016;12:1561–1570.
34. Suki B, Stamenovic D, Hubmayr R. Lung parenchymal mechanics. *Compr Physiol*. 2011;1:1317–1351.
35. Liu F, Mih JD, Shea BS, et al. Feedback amplification of fibrosis through matrix stiffening and COX-2 suppression. *J Cell Biol*. 2010;190:693–706.
36. Kallel F, Bertrand M. Tissue elasticity reconstruction using linear perturbation method. *IEEE Trans Med Imaging*. 1996;15:299–313.
37. Booth AJ, Hadley R, Cornett AM, et al. Acellular normal and fibrotic human lung matrices as a culture system for in vitro investigation. *Am J Respir Crit Care Med*. 2012;186:866–876.
38. Fu D, Levinson SF, Gracewski SM, Parker KJ. Non-invasive quantitative reconstruction of tissue elasticity using an iterative forward approach. *Phys Med Biol*. 2000;45:1495–1509.
39. Kemerink GJ, Lamers RJ, Pellis BJ, Kruize HH, van Engelshoven JM. On segmentation of lung parenchyma in quantitative computed tomography of the lung. *Med Phys*. 1998;25:2432–2439.
40. Elaiyaraja G, Kumaratharan N. An enhanced algorithm for removal of noise in CT scan image and 3D abdomen color video sequence through trimmed based filter. *Biomed Res-India*. 2017;28:512–518.
41. Qing K, Altes TA, Tustison NJ, et al. Rapid acquisition of helium-3 and proton three-dimensional image sets of the human lung in a single breath-hold using compressed sensing. *Magn Reson Med*. 2015;74:1110–1115.
42. Bognar G. Image quality measurement for low-dose human lung CT scans. In: *2015 38th International Conference on Telecommunications and Signal Processing (Tsp)*; 2015: 587–591.
43. Wang Z, Bovik AC, Sheikh HR, Simoncelli EP. Image quality assessment: from error visibility to structural similarity. *IEEE Trans Image Process*. 2004;13:600–612.
44. Zhao F, Huang QM, Gao W. Image matching by normalized cross-correlation. In: *2006 IEEE International Conference on Acoustics, Speech and Signal Processing*, Vols 1-13; 2006: 1977–1980.
45. Avants BB, Epstein CL, Grossman M, Gee JC. Symmetric diffeomorphic image registration with cross-correlation: evaluating automated labeling of elderly and neurodegenerative brain. *Med Image Anal*. 2008;12:26–41.
46. Viola P, Wells WM. Alignment by maximization of mutual information. *Int J Comput Vision*. 1997;24:137–154.
47. Modat M, Vercauteren T, Ridgway GR, et al. Diffeomorphic demons using normalised mutual information, evaluation on multi-modal brain MR images. In: *Medical Imaging 2010: Image Processing*; 2010: 7623.
48. Foundation PS. *Python 2.7*. 2017: <https://www.python.org/>
49. Papandrinopoulou D, Tzouda V, Tsoukalas G. Lung compliance and chronic obstructive pulmonary disease. *Pulm Med*. 2012;2012:542769.
50. Yamamoto T, Kabus S, Bal M, et al. The first patient treatment of computed tomography ventilation functional image-guided radiotherapy for lung cancer. *Radiother Oncol*. 2016;118:227–231.
51. Yamamoto T, Kabus S, Lorenz C, et al. Pulmonary ventilation imaging based on 4-dimensional computed tomography: comparison with pulmonary function tests and SPECT ventilation images. *Int J Radiat Oncol Biol Phys*. 2014;90:414–422.
52. Kida S, Bal M, Kabus S, et al. CT ventilation functional image-based IMRT treatment plans are comparable to SPECT ventilation functional image-based plans. *Radiother Oncol*. 2016;118:521–527.
53. Kimura T, Nishibuchi I, Murakami Y, et al. Functional image-guided radiotherapy planning in respiratory-gated intensity-modulated radiotherapy for lung cancer patients with chronic obstructive pulmonary disease. *Int J Radiat Oncol Biol Phys*. 2012;82:e663–e670.